High-performance enhancement-mode thin-film transistors based on Mg-doped In$_2$O$_3$ nanofiber networks

Hongchao Zhang[1], You Meng[1], Longfei Song[1], Linqu Luo[1], Yuanbin Qin[2], Ning Han[3], Zaixing Yang[4], Lei Liu[1], Johnny C. Ho[5,6,7] (✉), and Fengyun Wang[1] (✉)

[1] *College of Physics and Cultivation Base for State Key Laboratory, Qingdao University, Qingdao 266071, China*

[2] *Center for Advancing Materials Performance from the Nanoscale, State Key Laboratory for Mechanical Behavior of Materials, Xi'an Jiaotong University, Xi'an 710049, China*

[3] *State Key Laboratory of Multiphase Complex Systems, Institute of Process Engineering, Chinese Academy of Sciences, Beijing 100190, China*

[4] *School of Microelectronics and Center of Nanoelectronics, Shandong University, Jinan 250100, China*

[5] *Department of Materials Science and Engineering, City University of Hong Kong, 83 Tat Chee Avenue, Kowloon, Hong Kong, China*

[6] *State Key Laboratory of Millimeter Waves, City University of Hong Kong, 83 Tat Chee Avenue, Kowloon, Hong Kong, China*

[7] *Shenzhen Research Institute, City University of Hong Kong, Shenzhen 518057, China*

ABSTRACT

Although In$_2$O$_3$ nanofibers (NFs) are well-known candidates as active materials for next-generation, low-cost electronics, these NF based devices still suffer from high leakage current, insufficient on–off current ratios (I_{on}/I_{off}), and large, negative threshold voltages (V_{TH}), leading to poor device performance, parasitic energy consumption, and rather complicated circuit design. Here, instead of the conventional surface modification of In$_2$O$_3$ NFs, we present a one-step electrospinning process (i.e., without hot-press) to obtain controllable Mg-doped In$_2$O$_3$ NF networks to achieve high-performance enhancement-mode thin-film transistors (TFTs). By simply adjusting the Mg doping concentration, the device performance can be manipulated precisely. For the optimal doping concentration of 2 mol%, the devices exhibit a small V_{TH} (3.2 V), high saturation current (1.1 × 10^{-4} A), large on/off current ratio (> 10^8), and respectable peak carrier mobility (2.04 cm^2/(V·s)), corresponding to one of the best device performances among all 1D metal-oxide NFs based devices reported so far. When high-κ HfO$_x$ thin films are employed as the gate dielectric, their electron mobility and V_{TH} can be further improved to 5.30 cm^2/(V·s) and 0.9 V, respectively, which demonstrates the promising prospect of these Mg-doped In$_2$O$_3$ NF networks for high-performance, large-scale, and low-power electronics.

Address correspondence to Fengyun Wang, fywang@qdu.edu.cn; Johnny C. Ho, johnnyho@cityu.edu.hk

1 Introduction

In recent years, one-dimensional (1D) semiconductor nanofibers (NFs) have attracted extensive attention due to their superior physical and chemical properties, including their distinctive transport characteristics, enormous surface-to-volume ratio, excellent mechanical flexibility, ease of fabrication, and so on [1–7]. All these extraordinary properties would offer enticing possibilities of using NFs for various high-performance, cost-effective technological applications. Among many promising candidate materials, In_2O_3 NFs are widely considered as the ideal channel materials for next-generation displays [8, 9] and electronics [10–12], arising from their chemical stability, optical transparency, and high carrier mobility (μ_{fe}); however, most of these In_2O_3 NFs based field-effect transistors (FETs) generally suffer from high leakage current and substantial negative threshold voltages (V_{TH}), which is attributed to the residual excess carrier concentration within NFs [13]. This significant negative V_{TH} implies that there is always a non-zero channel current at zero gate bias, in which such devices would then be operated in the accumulation or depletion mode (D-mode) [14]. Conversely, enhancement mode (E-mode) devices typically consist of a small positive V_{TH} and exhibit a negligible off-current at zero gate bias, which are highly preferred for simple, low-power, and large-scale electronic circuit integration since there is no need to apply any gate voltage to switch off the transistors [15, 16]. In any case, although the E-mode NF devices with suitable off-current have illustrated many distinctive advantages, achieving high-performance E-mode thin-film transistors (TFTs) based on In_2O_3 NFs still remains an important challenge.

In order to tackle the aforementioned challenges, several strategies have been established to alter the electrical properties of transistors made of 1D metal-oxide channel materials, such as chemical vapor deposition (CVD) grown nanowires (NWs) [17], while limited reports have focused on electrospun NFs [18, 19]. One technique is to manipulate the surface architecture of NW channels in order to modulate their corresponding free carrier concentration. For instance, different surface passivation schemes have been developed to vary the electrical properties of

In_2O_3 NW FETs [20]. Moreover, D-mode ZnO NWs based devices have also been fabricated utilizing smooth NW channels, whereas the device operation mode would change to E-mode accordingly when surface-corrugated NWs are used for the channel [21]. Another approach concentrates on employing different metal dopants to compensate for the oxygen vacancies of In_2O_3 NWs by reducing their free carrier concentration and eventually shifting the V_{TH} positively to attain E-mode FETs [22]. Unfortunately, neither solves the problem completely due to their associated drawbacks. Specifically, NW surface modulation may be difficult for large-scale device integration because of the wire-to-wire variation of their exposed surfaces. The metal-doping of NWs seems applicable only to a single NW device channel, but practical devices usually require large-area, uniform, and dense NW arrays. Fabricating such NW arrays through a combination of processes in catalytic CVD [17, 23], NW printing [24], and device construction [25] may be uneconomical. In contrast, for practical transistor and circuit integration, electrospun NFs are much more favorable than CVD grown NWs for active device channels due to the simplicity of the electrospinning process and capability to be directly deposited on the device substrate [26–29]. ZnO NFs and In_2O_3-ZnO-$ZnGa_2O_4$ composite NF networks have been successfully fabricated as device channels and integrated with silicon to achieve FETs with impressive transistor parameters [30, 31]. For device performance enhancement, a post-spinning hot-pressing step is also developed to address the notorious problem of poor interfacial adhesion between the metal-oxide NFs and gate oxide layer [31]. In addition, well-aligned ZnO NF parallel arrayed device channels have recently been fabricated using electrospinning with a high degree of alignment and control over the fiber spacing, which are advantageous for rapid and scalable device fabrication; nevertheless, the relatively low on-current density, large V_{TH}, and insufficient on/off current ratio of fabricated NF arrayed devices would still greatly restrict their large-scale deployment [32]. In this regard, it is essential to achieve reliable control over the electron transport properties of metal-oxide NF devices.

In this study, we present a versatile and one-step electrospinning process (i.e., without hot-press) to

obtain controllable Mg-doped In_2O_3 NF networks to realize high-performance E-mode TFTs. Importantly, by adjusting the Mg doping concentration from 0 to 6 mol%, all the device parameters of fabricated TFTs could be manipulated precisely. For the optimal Mg doping concentration of 2 mol%, the devices exhibited E-mode operation with a small V_{TH} of 3.2 V, high saturation current of 1.1×10^{-4} A, large on/off current ratio of $> 10^8$, and respectable peak μ_{fe} of 2.04 $cm^2/(V \cdot s)$, corresponding to one of the best device performances among all 1D metal-oxide NFs based devices reported so far [13, 31]. When a high-κ thin-film of HfO_x is employed as the gate dielectric, the electron mobility and V_{TH} of the constructed TFTs could be further improved to 5.30 $cm^2/(V \cdot s)$ and 0.9 V, respectively. As such, Mg-doped In_2O_3 NF network TFTs are promising prospects for high-performance, E-mode, large-area, and advanced electronic devices.

2   Experimental

2.1   Preparation of the precursor

Both bare and Mg-doped In_2O_3 NFs were prepared by the conventional electrospinning process, followed by UV/ozone treatment and calcination. Typically, 2 g of polyvinyl pyrrolidine (PVP, M_W of 1,300,000 g/mol, Aladdin), 0.4 g of indium chloride tetrahydrate ($InCl_3 \cdot 4H_2O$, 99.9%, Aladdin), and varied amounts from 0.002 to 0.016 g of magnesium nitrate hexahydrate ($Mg(NO_3)_2 \cdot 6H_2O$, 99.9%, Aladdin) were mixed together with 10 g of dimethyl formamide (DMF, 99.8%, Aladdin) in a small bottle. The finished solution was then maintained under vigorous magnetic stirring for 8 h to form a viscous gel, which would then serve as the precursor for Mg-doped In_2O_3 NFs. The Mg doping concentration was controlled from 1 mol% to 6 mol%, corresponding to the mole ratio of Mg (mole(Mg)/[mole(Mg) + mole(In)]). The undoped In_2O_3 NF precursor was prepared the same way as that for the Mg-doped In_2O_3 NFs, except without adding $Mg(NO_3)_2 \cdot 6H_2O$ as dopant.

2.2   Preparation of bare and Mg-doped In_2O_3 NFs

The prepared precursors were next electrospun into Mg-doped In_2O_3 and undoped In_2O_3 NFs, respectively,

at room temperature (20 °C) with a relative humidity of 40%. The precursor solution was first loaded into a syringe, and the syringe needle was connected to the anode of the direct-current high-voltage power supply. A piece of heavily doped p-type Si substrate with thermally grown SiO_2 gate dielectric (100 nm thick) was placed perpendicular to the needle tip at a 15-cm distance to act as a collector and was connected to the ground. An electric potential of 15 kV was applied between the needle and the collector by a high-voltage power supply, and the NFs were obtained on the collector with a spinning time of 30 s (the density of the NFs was 0.43 pillars/μm).

2.3   Fabrication of NFs-based FETs

In order to enhance the interface adhesion properties for electrospun nanofiber FETs to improve the gate coupling effect, electrical performance, and operational stability of the FETs, the as-spun composite NF networks were baked at 150 °C for 10 min and then were treated using a high-pressure mercury UV lamp for 40 min. The UV lamp power was 1 kW, and the wavelengths of the lamp were 290–320 nm. After that, the NFs were thermally annealed at 600 °C for 1 h in air to remove the organic components of PVP, forming crystalline Mg-doped In_2O_3 or undoped In_2O_3 NFs. Finally, an Al source and drain electrodes were deposited by thermal evaporation using a shadow mask with the channel width and length of 1,000 and 100 μm, respectively.

2.4   Fabrication of 2 mol% Mg-In_2O_3/HfO_x NFs-based FETs

To fabricate the electrospun 2 mol% Mg-In_2O_3 FETs with a high-κ dielectric layer, HfO_x thin films were prepared by a solution process. The 0.1 M HfO_x precursor solution was prepared through dissolving hafnium (IV) tetrachloride ($HfCl_4$, 98%, Aldrich, USA) in 2-methoxyethanol (99.9%, Aladdin) and then stirred for 12 h. The precursor solution was next filtered through a 0.22-μm polytetrafluoroethylene (PTFE) syringe filter. A heavily doped p-type Si substrate was also prepared by sequential ultrasonic cleaning in acetone, ethanol, and deionized (DI) water and blow-dried by an N_2 gun. The filtered precursor solution

was then spin-coated on the Si substrate at a speed of 300 rpm for 5 s and 6,000 rpm for 15 s. After that, the samples were dried at 150 °C on a hot plate for 10 min to cure the thin film and were thermally annealed at 600 °C for 120 min. The other processes such as 2 mol% Mg-In_2O_3 electrospinning and integration of the TFT device were the same as above.

2.5 Characterization

The morphology of the electrospun NFs was observed by using scanning electron microscopy (SEM, Nova Nano SEM450, operated at 15 keV). The crystal structure of the NFs was also characterized by X-ray diffraction (XRD, Rigaku D/max-rB). The microstructure of the NFs was determined by analyzing the transmission electron microscopy (TEM) images and reciprocal lattice spots extracted from the fast Fourier transform (FFT) with a high-resolution transmission electron microscope (HRTEM, JEOL JEM 2100F, operated at 200 kV). Energy dispersive X-ray spectroscopy (EDS, Oxford Instrument and EDAX Inc, attached to the HRTEM) was used to analyze the composition (e.g., doping concentration) and elemental distribution of obtained Mg-doped In_2O_3 NFs. The electrical properties of fabricated FETs employing Mg-doped In_2O_3 and undoped In_2O_3 NFs as the device channel were measured under ambient conditions using a semiconductor parameter analyzer (Keithley 2634B) and probe station.

3 Results and discussion

Representative SEM images of undoped and 2 mol%, 4 mol%, 6 mol% Mg-doped In_2O_3 NFs before UV irradiation and calcination are shown in Figs. S1(a)–S1(d) in the Electronic Supplementary Material (ESM); clearly, the as-spun NFs could be collected on substrates aligned in a randomly oriented network due to the bending instability of the whipping process. Utilizing the same optimal electrospinning conditions, all obtained NFs were straight and long with a smooth surface and uniform diameter along their entire length. The diameter distribution ranged from 300 to 500 nm, and their length was from 10 to 100 μm. The collected NFs were then treated with UV and calcinated to convert them into In_2O_3 NFs. After calcination, the NFs maintained their continuous structure (Figs. 1(a) and 1(b), and Figs. S1(e) and S1(f) in the ESM), while their diameter decreased to 80 ± 8.5 and 80.1 ± 9.2 nm for the undoped and 2 mol% Mg-doped In_2O_3 NFs, respectively, based on the statistics of more than 100 NFs for both samples (Figs. S2(a)–S2(d) in the ESM). The diameters decreased mainly because of the loss of PVP from the NFs and crystallization of In_2O_3. The insets of Figs. 1(a) and 1(b) present the zoomed-in SEM images of individual NFs of the undoped and 2 mol% Mg-doped In_2O_3 after annealing. As observed, the NF surface became coarser with the addition of Mg dopant, while the incorporation of dopant atoms induced negligible effects on the NF morphology. Notably, the dopant concentration did not contribute any noticeable influence on the NF diameter, distribution, or coverage (i.e., the density of fibers within the network) obtained on the substrate (Fig. S1 in the ESM). All these parameters' uniformity are essential for fair and consistent comparison in the subsequent studies of the obtained NFs. In order to investigate the effect of Mg doping concentration on the electron
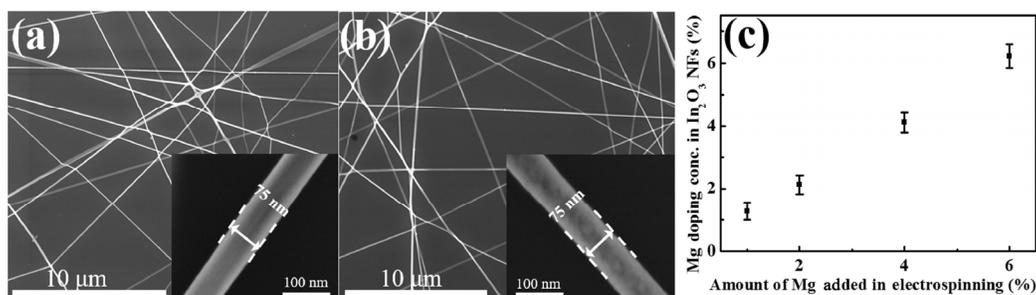
Figure 1 SEM images of (a) undoped In_2O_3 NFs and (b) 2 mol% Mg-doped In_2O_3 after annealing at 600 °C for 1 h. Insets in (a) and (b) are SEM images of a single undoped In_2O_3 NF and 2 mol% Mg-doped In_2O_3 NF, respectively. (c) The statistics of the mole fraction of Mg (mole(Mg)/[mole(In) + mole(Mg)]) determined by EDS spectra for more than 20 NFs versus the originally added values of Mg concentration, indicating the Mg elements have been successfully doped into In_2O_3 NFs.

transport properties of In_2O_3 NFs, different amounts of $InCl_3 \cdot 4H_2O$ and $Mg(NO_3)_2 \cdot 6H_2O$ were added to the precursor solution to reach 1 mol%, 2 mol%, 4 mol%, and 6 mol% Mg mole ratios, which are defined by the following formula

Mg mol% = mole(Mg)/(mole(In) + mole(Mg))　　　(1)

As shown in Fig. 1(c), the Mg concentration of the as-fabricated NFs increases with increasing of Mg content added in the precursor, which is consistent with the results determined by EDS. For each Mg doping concentration, more than twenty NFs were randomly chosen for an EDS point scan in the NF body. Figures S3(a)–S3(e) in the ESM show represen-tative EDS spectra of 0, 1 mol%, 2 mol%, 4 mol%, and 6 mol% Mg-doped In_2O_3 NFs. Evidently, when the concentration of Mg increases, the peak for Mg increases, and the exact Mg concentration was deter-mined by the quantitative analysis of EDS signals. The incorporation of Mg into the NFs could be further confirmed by performing detailed XRD analysis in the 2θ range between 20° and 50° (Fig. S4 in the ESM). The XRD spectra were taken from x mol% Mg doped In_2O_3 NFs, where x has values of 0, 1, 2, 4, and 6. Notably, all of the samples exhibited the cubic phase of In_2O_3 (JCPDS 06-0416), and no impurity peaks, such as metallic Mg, MgO, and/or $MgIn_2O_4$ phases, were observed. When the Mg doping concentration increased, the strongest (222) peaks were shifted towards a higher angle, revealing a narrowing of the lattice constant for the In_2O_3 crystal. This observation could be attributed to the introduction of Mg into the lattice sites of the In_2O_3 crystal since Mg has a smaller atomic or ionic radius than In. Consequently, the lattice becomes distorted, and ionized impurity scattering sites formed, which hamper the transport of carriers within the NFs. Additionally, the binding energy bet-ween Mg and O is larger than that between In and O. Therefore, Mg doping could effectively reduce the con-centration of O vacancies and thus eventually decreases the carrier concentration. As a result, the Mg doping could effectively influence the carrier concentration and their transport velocity in the In_2O_3 lattice [22, 33].

At the same time, detailed structural information of the 2 mol% Mg-doped In_2O_3 NF calcinated at 600 °C in

air for 1 h was analyzed by TEM. As shown in Fig. 2(a), a single Mg-In_2O_3 NF is continuous with relatively a coarse surface and fiber diameter of ~ 50 nm. Figure 2(b) provides the corresponding FFT pattern of the selected area as designated in Fig. 2(a), and the discontinuous diffraction rings indicate the multi-crystalline phase of Mg-In_2O_3. The HRTEM image further confirms the poly-crystalline nature of the fabricated Mg-In_2O_3 NFs (Fig. 2(c)). As depicted in Fig. 2(d), the lattice fringes display inter-planar spacings of 2.85 and 2.82 Å with an intersection angle of 68°, corresponding to the $(\bar{2}\bar{2}2)$ and $(2\bar{2}2)$ planes of cubic In_2O_3 $(\bar{2}\bar{2}2)$, respectively. All these confirmed the observed slight reduction in the In_2O_3 lattice constant (e.g., from 2.92 to 2.85 Å for the $(\bar{2}\bar{2}2)$ plane), which agreed well with the XRD measurements. In addition, elemental mapping was also performed and is pre-sented in Fig. 3 to evaluate the doping uniformity of Mg. Specifically, Figs. 3(b)–3(d) demonstrate the homogenous distribution of O, Mg, and In atoms along the NF body axially and radially. These observations
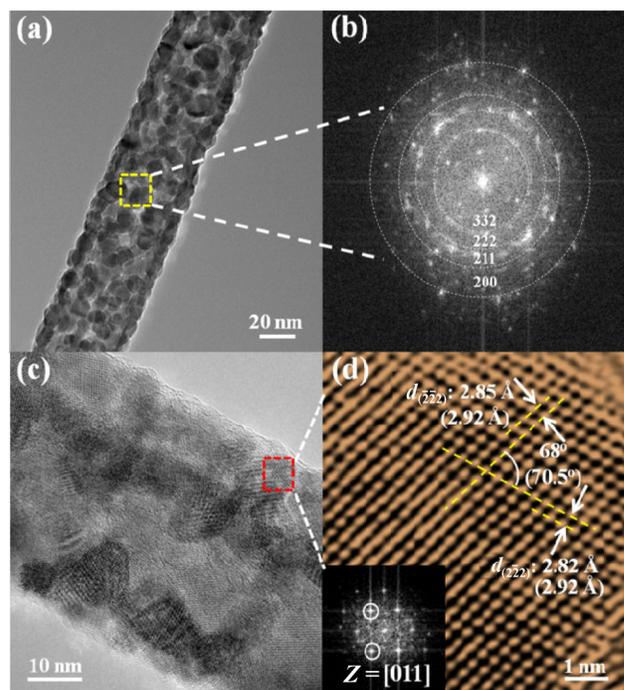
Figure 2 (a) TEM image of a 2 mol% Mg-doped In_2O_3 NF (d = 75 nm). (b) FFT and (c) HRTEM images of the selected area marked with a yellow rectangle in (a), exhibiting polycrystalline properties. (d) HRTEM image of the area highlighted with a red rectangle in (c) and inset of the relative FFT image, illustrating the cubic zinc-blend crystal structure of In_2O_3.
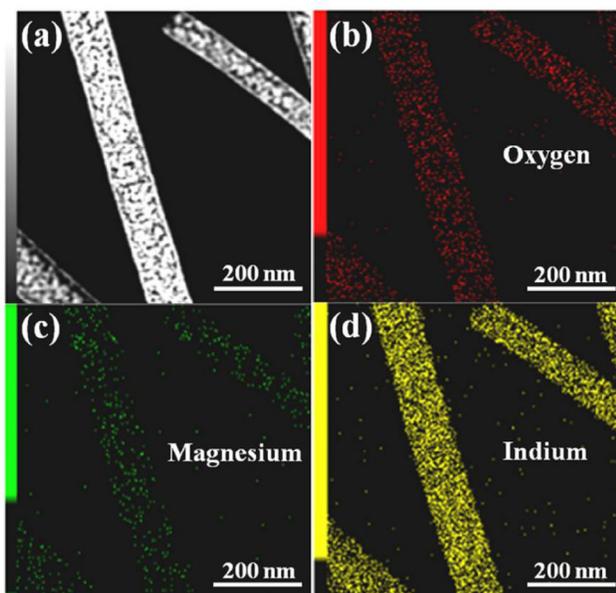
Figure 3 (a) Dark-field image of the 2 mol% Mg-doped In_2O_3 NFs and the corresponding EDS elemental mapping of (b) O, (c) Mg, and (d) In, illustrating the homogeneous distribution of In, Mg, and O atoms along the NF body.

demonstrated that electrospinning could achieve high-quality In_2O_3 NFs with controlled doping concentrations and uniformity.

In order to investigate the electrical properties of these In_2O_3 NFs, FETs were fabricated utilizing un-doped and Mg-In_2O_3 NF networks with doping concentrations of 1 mol%, 2 mol%, 4 mol%, and 6 mol% as the channel materials. Figure 4(a) illustrates the SEM image of a typical In_2O_3 NF networked FET and a schematic illustration configured in the global back-gated geometry. Explicitly, the density of In_2O_3 NF networks was estimated to be 0.43 NFs/μm with the electrospinning time of 30 s employed in this work. This density would result in the best electrical performance among all investigated devices. When the NF density is low, insufficient channel coverage would lead to small output current and poor carrier mobility [13, 34]. When the density is too high, even though the current continues to increase, the corresponding switching characteristic and on/off current ratio become degraded, restricting the practical use of NF devices [13, 34]. Importantly, all devices were fabricated using the same process conditions, device geometry, and materials, except for the Mg doping concentration. The same gate voltage (V_{GS}) sweep rate

was also employed to ensure a consistent comparison among all the devices characterized. Figure 4(b) shows representative transfer curves measured by sweeping V_{GS} from –30 to 30 V at source to drain voltage (V_{DS}) = 30 V for Mg doping concentrations of 0, 1 mol%, 2 mol%, 4 mol%, and 6 mol%. All of them exhibited classical n-type electrical behavior as anticipated. For the undoped In_2O_3 NF device, a high off-current of 5×10^{-7} A, low on–off current ratio (I_{on}/I_{off}) value of ~ 520, and large negative V_{TH} of –28.3 V were observed. The V_{TH} value can be directly obtained from the horizontal intercept of the linear regimes in the square root of source to drain current ($I_{DS}^{1/2}$) vs. V_{GS} curves as presented in Fig. 4(c). The negative V_{TH} suggested that the device would yield a nonzero current at zero gate bias, which leads to elevated power consumption. Regardless, this poor device performance could be attributed to the uncontrolled excess carrier concentration in the In_2O_3 NFs [13]. These carriers typically originate from the oxygen vacancies behaving as donor-like defects [18], preventing reliable control of the electrical properties of In_2O_3 NF devices. In this case, since Mg has a lower standard electrode potential (E_o = –2.37 V) than In (E_o = –0.34 V), Mg could be more easily ionized and thus could strongly bind with oxygen to form MgO with a larger band gap (~ 7.9 eV) than In_2O_3 [35]. In this manner, when Mg atoms were incorporated into the In_2O_3 NF lattice, a certain number of oxygen vacancies would be consumed, which reduced the excess carrier concentration. Thus, various amounts of Mg were doped into In_2O_3 NFs in order to modulate their carrier concentration and corresponding electrical properties. As shown in Fig. 4(b), the off-current decreased significantly with increasing Mg concentration. For instance, the 2 mol% Mg-doped In_2O_3 NF device displayed an off-current down to 10^{-12} A, which is about five orders of magnitude lower than that of pristine In_2O_3 NFs. Furthermore, values for V_{TH} of –28.3, –3.3, 3.2, 7.3, and 15.1 V could be determined for NF devices with Mg doping concentrations of 0, 1 mol%, 2 mol%, 4 mol%, and 6 mol%, respectively (Fig. 4(c)). Therefore, increasing Mg doping could reliably deplete the excess carrier concentration of In_2O_3 NFs and could remarkably shift V_{TH} towards the positive values necessary for E-mode device characteristics. Nonetheless, when the doping amount became too high, the on-current would considerably
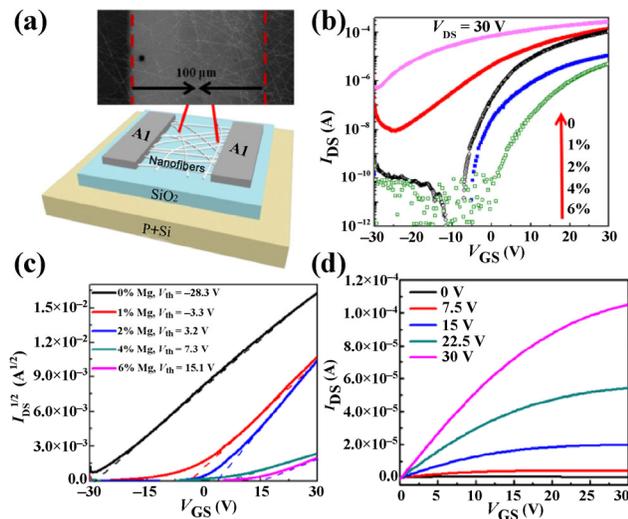
Figure 4 (a) (Top) SEM image and (bottom) schematic of a back-gated Mg-doped In_2O_3 NF FETs fabricated with Al electrodes and heavily doped silicon substrates covered with 150 nm thick thermally grown SiO_2. The SEM image illustrates the density of Mg-doped In_2O_3 NFs in the channel and when the density was 0.43 pillars/μm (spinning time of 30 s); the Mg-doped In_2O_3 NF FETs show the best performance. (b) Transfer curves for the back-gated FETs with different Mg doping concentrations (0, 1 mol%, 2 mol%, 4 mol%, and 6 mol%). (c) $I_{DS}^{1/2}$ versus V_{GS} curves for the back-gated FET with different Mg doping concentrations (0, 1 mol%, 2 mol%, 4 mol%, and 6 mol%), demonstrating the D-mode FET being successfully transformed into an E-mode one. (d) Output curves of 2 mol% Mg-doped In_2O_3 NF FETs.

decrease from 2.6×10^{-4} A (0) to 5.0×10^{-6} A (6 mol%) due to the lack of carriers for electrical conduction. Regardless, for the Mg doping concentration of 2 mol%, the In_2O_3 NF network based device could be successfully transformed to E-mode (i.e. $V_{TH} = 3.2$ V) operation with impressive electrical properties, including a high saturation current of 1.1×10^{-4} A, excellent I_{on}/I_{off} ratio of ~ 10^8, and decent peak μ_{fe} of 2.02 cm²/(V·s) with a gate voltage of 30 V and drain voltage of 30 V. In addition, based on the device output characteristics (Fig. 4(d) and Fig. S5 in the ESM), the output current (I_{DS}) saturates at the high source/drain bias (V_{DS}) and increases linearly with V_{DS} at low V_{DS}. This linear-to-saturation operation could be ascribed to the formation of ohmic-like contacts between the Al electrodes and NF channels. The I_{DS} saturation along with pinch-off also suggested that the carrier transport was well controlled by the gate bias. All these results established that the optimal Mg doping concentration was 2 mol%

for effective V_{TH} manipulation without sacrificing the other device parameters.

Moreover, a statistical analysis was also carried out to further understand and connect the changes in V_{TH}, on-current, and other device parameters to the Mg doping concentration of fabricated NF transistors. The average and standard deviation of these parameters were calculated based on 10 In_2O_3 NF network based FETs with different doping content for each sample group. As depicted in Fig. 5(a), the average V_{TH} value ranged from −26.5 to 11.7 V as the Mg concentration increased from 0 to 6 mol%. This positive V_{TH} shift was believed to be induced by the reduced carrier concentration (n), which can be calculated by the following equation [22]

$$n = \frac{4C_i(V_{GS} - V_{TH})}{\pi q d^2 L} \qquad (2)$$

where C_i is the areal capacitance of the dielectric (i.e., SiO_2), q is the electronic charge, d is the NF diameter, and L is the NF device channel length (i.e., 10 μm). According to Eq. (2), due to the inversely proportional relationship between n and V_{TH}, when the Mg doping concentration increases, the V_{TH} increases, and the carrier concentration decreases accordingly. The field-effect mobility (μ_{fe}) can be calculated from the transfer characteristics using the following equation [36]
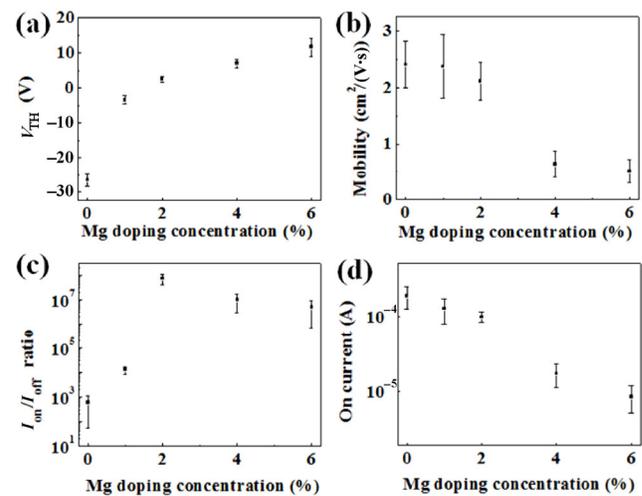
Figure 5 Average (a) V_{TH}, (b) mobility, (c) I_{on}/I_{off} ratio, and (d) on current of 50 NF devices versus Mg doping concentration (0, 1 mol%, 2 mol%, 4 mol%, and 6 mol%).

$$I_{DS} = \left(\frac{W}{2L}C_i\mu_{fe}\right)(V_{GS} - V_{TH})^2 \qquad (3)$$

where W and L are the channel width and length of the device, respectively, and V_{GS} is the gate voltage employed (30 V). The average μ_{fe} values could be then estimated to be 2.41, 2.38, 2.12, 0.64 and 0.51 cm²/(V·s) for Mg doping concentrations of 0, 1 mol%, 2 mol%, 4 mol%, and 6 mol%, respectively (Fig. 5(b)). This degradation of μ_{fe} is perfectly consistent with the lattice distortion and ionized impurities discussed above. Meanwhile, the off-current remarkably decreased from 5×10^{-7} to 10^{-12} A, and thus the I_{on}/I_{off} ratio significantly improved from 10^3 to 10^8, when the Mg doping concentration increased from 0 to 2 mol% (Fig. S6(a) in the ESM and Fig. 5(c)). Simultaneously, only a small amount on-current was sacrificed with a small decrease from 1.8×10^{-4} to 1×10^{-4} A (Fig. 5(d)). When the Mg doping concentration was optimized at 2 mol%, the devices were also observed to have the highest on/off ratio (i.e., 10^8) and an impressive SS value (i.e., 290 mV/dec, Fig. S6(b) in the ESM). All these demonstrate the great potential of this metal doping approach for the future low-operating-power, high-performance, NFs-based electronics and optoelectronics.

Although an impressive electrical device performance has been achieved for the FETs based on Mg-In₂O₃ NF networks, a relatively large gate voltage of 30 V is still required for device operation, which significantly restricts the practical use of these NF devices. To further improve the electrical properties of the optimal Mg-doped In₂O₃ NF devices (i.e., 2 mol%), the high-κ dielectric of hafnium oxide (HfO$_x$) thin films was fabricated by a solution process and integrated into the NF devices [37]. Among various high-κ dielectrics, HfO$_x$ has been singled out due to its high dielectric constant ($\kappa \sim 25$–30), wide band gap (5.68 eV), and large conduction band offset of 1.4 eV, which are the key criteria for device performance enhancement. As depicted in the device schematic in Fig. 6(a), the HfO$_x$ films were deposited with a thickness of ~ 12 nm and capacitance of ~ 300 nF/cm² and were incorporated as a dielectric layer in the global back-gated configuration [38]. The film surface was observed to be smooth as produced by the solution technique (data not shown), which was beneficial for the formation of a high-quality and conformal interface with the NF device channel. When the V_{DS} was set at 3 V and was swept from –1 to 5 V, the on-current and off-current of the fabricated device were found to be 1.8×10^{-5} A and 10^{-11} A, respectively, resulting in an I_{on}/I_{off} ratio of 1.8×10^{-6}. The μ_{fe} value could also be estimated in the saturation region, which was 5.3 cm²/(V·s). The corresponding output curves also present its superior gate-modulated device characteristics. A good I_{DS} saturation was observed even at the lower operating voltage (< 5 V) (Figs. 6(b) and 6(c)). The electrical properties of the undoped In₂O₃ NF/SiO₂ device, 2 mol% Mg-In₂O₃ NF/SiO₂ device, and 2 mol% Mg-In₂O₃ NF/HfO$_x$ device are summarized in Table S1 in the ESM. Evidently, the consequent device V_{TH}, off-current, and I_{on}/I_{off} ratio could be effectively modulated by optimal Mg doping in the In₂O₃ NFs with negligible changes in other electrical properties, such as subthreshold slope (SS), μ_{fe}, and on-current. The introduction of high-κ dielectric HfO$_x$ thin films could further decrease the operating gate and drain voltages of the NF device from 30 to 5 V and from 30 to 2 V, respectively, and improve μ_{fe} by
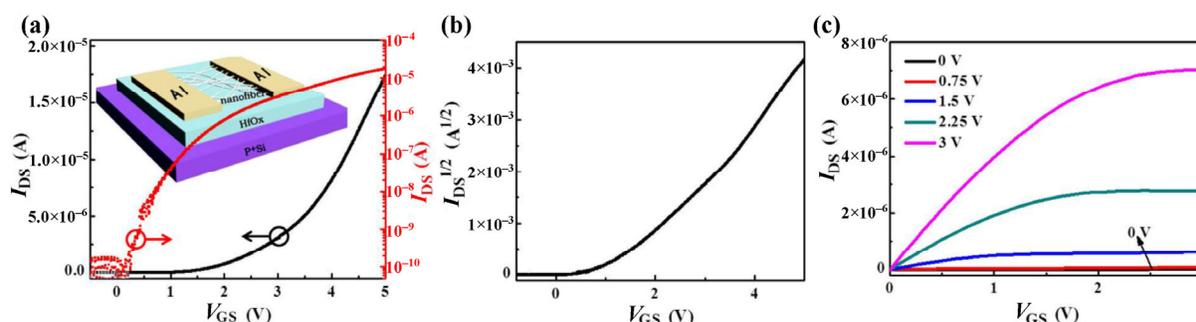
Figure 6 (a) Transfer curves ($V_{DS} = 2$ V). (b) $I_{DS}^{1/2}$ versus V_{GS} curves and (c) output of 2 mol% Mg-doped In₂O₃ NF FETs with high-κ dielectric material (HfO$_x$) and V_{DS} from 0 to 3 V, showing a low operating voltage (5 V) and an appropriate V_{TH} (0.9 V). The inset is the schematic structure of a back-gated 2 mol% Mg-doped In₂O₃ NFs FET.

more than 2 times to reduce the energy consumption. More importantly, the V_{TH} could be reduced to only 0.9 V, which was in distinct contrast to the device with the SiO_2 dielectric layer. In the future, their device performance could still be substantially improved by optimizing the areal NF network coverage in the device channel, adopting NF parallel arrays, reducing the channel length, and/or employing a top-gated device structure. All these findings clearly indicate the technological potency of these Mg-In_2O_3 NFs for high-performance and low-power electronic devices.

4   Conclusions

In summary, we have successfully fabricated low-operating-power and high-performance enhancement-mode transistors based on Mg-doped In_2O_3 NF networks, in which the NFs are readily fabricated by a simple one-step electrospinning method. Importantly, the electrical properties of these NFs can be effectively controlled and tailored by varying the Mg doping concentration. When the Mg doping concentration is controlled at 2 mol%, the In_2O_3 NF device exhibit impressive enhancement-mode device performance with a relatively small V_{TH} of 3.2 V, high saturation current of 1.1×10^{-4} A, high I_{on}/I_{off} ratio of ~ 10^8, and high peak μ_{fe} of 2.04 cm^2/(V·s). Moreover, combined with a high-κ solution-processed HfO$_x$ gate insulator, the operating gate and drain voltages can be further lowered to < 5 and 2 V, respectively, while superior values for μ_{fe} of 5.3 cm^2/(V·s) and V_{TH} of 0.9 V are obtained. All these demonstrate the great potential implications of these NFs for future large-scale nano-electronics, sensors, and other applications.

Acknowledgements

Electronic Supplementary Material: Supplementary material (SEM pictures, diameter statistics, XRD, EDS measurements, output curves of the pure In_2O_3 NFs FET, the average of off current and SS values and Table S1 for electrical parameters summary) is available in the online version of this article at https://doi.org/10.1007/s12274-017-1735-8.

References

[1] Huang, Y.; Duan, X. F.; Cui, Y.; Lauhon, L. J.; Kim, K. H.; Lieber, C. M. Logic gates and computation from assembled nanowire building blocks. *Science* **2001**, *294*, 1313–1317.

[2] Chuang, S.; Gao, Q.; Kapadia, R.; Ford, A. C.; Guo, J.; Javey, A. Ballistic InAs nanowire transistors. *Nano Lett*. **2012**, *13*, 555–558.

[3] Razavieh, A.; Mehrotra, S.; Singh, N.; Klimeck, G.; Janes, D.; Appenzeller, J. Utilizing the unique properties of nanowire MOSFETs for RF applications. *Nano Lett*. **2013**, *13*, 1549–1554.

[4] Duan, X. F.; Niu, C. M.; Sahi, V.; Chen, J.; Parce, J. W.; Empedocles, S.; Goldman, J. L. High-performance thin-film transistors using semiconductor nanowires and nanoribbons. *Nature* **2003**, *425*, 274–278.

[5] Li, Y.; Qian, F.; Xiang, J.; Lieber, C. M. Nanowire electronic and optoelectronic devices. *Mater*. *Today* **2006**, *9*, 18–27.

[6] Thelander, C.; Agarwal, P.; Brongersma, S.; Eymery, J.; Feiner, L. F.; Forchel, A.; Scheffler, M.; Riess, W.; Ohlsson, B. J.; Gösele, U. et al. Nanowire-based one-dimensional electronics. *Mater*. *Today* **2006**, *9*, 28–35.

[7] Ko, H.; Zhang, Z. X.; Ho, J. C.; Takei, K.; Kapadia, R.; Chueh, Y. L.; Cao, W. Z.; Cruden, B. A.; Javey, A. Flexible carbon-nanofiber connectors with anisotropic adhesion properties. *Small* **2010**, *6*, 22–26.

[8] Ju, S; Li, J. F.; Liu, J.; Chen, P. C.; Ha, Y. G.; Ishikawa, F.; Chang, H.; Zhou, C. W.; Facchetti, W. A.; Janes, D. B. et al. Transparent active matrix organic light-emitting diode displays driven by nanowire transistor circuitry. *Nano Lett*. **2008**, *8*, 997–1004.

[9] Ju, S.; Facchetti, A.; Xuan, Y.; Liu, J.; Ishikawa, F.; Ye, P. D.; Zhou, C. W.; Marks, T. J.; Janes, D. B. Fabrication of fully

transparent nanowire transistors for transparent and flexible electronics. *Nat. Nanotechnol.* **2007**, *2*, 378–384.

[10] Lee, C.; Srisungsitthisunti, P.; Park, S.; Kim, S.; Xu, X. F.; Roy, K.; Janes, D. B.; Zhou, C. W.; Ju, S.; Qi, M. H. Control of current saturation and threshold voltage shift in indium oxide nanowire transistors with femtosecond laser annealing. *ACS Nano* **2011**, *5*, 1095–1101.

[11] Li, C.; Zhang, D.; Han, S.; Liu, X.; Tang, T.; Zhou, C. Diameter-controlled growth of single-crystalline In_2O_3 nanowires and their electronic properties. *Adv. Mater.* **2003**, *15*, 143–146.

[12] Su, M.; Yang, Z. Y.; Liao, L.; Zou, X. M.; Ho, J. C.; Wang, J. L.; Wang, J. L.; Hu, W. D.; Xiao, X. H.; Jiang, C. Z. et al. Side-gated In_2O_3 nanowire ferroelectric FETs for high-performance nonvolatile memory applications. *Adv. Sci.* **2016**, *3*, 1600078.

[13] Park, H.; Yoon, K. R.; Kim, S. K.; Kim, I. D.; Jin, J.; Kim, Y. H.; Bae, B. S. Highly conducting In_2O_3 nanowire network with passivating ZrO_2 thin film for solution-processed field effect transistors. *Adv. Electron. Mater.* **2016**, *2*, 1600218.

[14] Ford, A. C.; Ho, J. C.; Chueh, Y. L.; Tseng, Y. C.; Fan, Z. Y.; Guo, J.; Bokor, J.; Javey, A. Diameter-dependent electron mobility of InAs nanowires. *Nano Lett.* **2009**, *9*, 360–365.

[15] Nikoobakht, B. Toward industrial-scale fabrication of nanowire-based devices. *Chem. Mater.* **2007**, *19*, 5279–5284.

[16] Xuan, Y.; Wu, Y. Q.; Ye, P. D. High-performance inversion-type enhancement-mode InGaAs MOSFET with maximum drain current exceeding 1 A/mm. *IEEE Electron Device Lett.* **2008**, *29*, 294–296.

[17] Zhu, Z. T.; Suzuki, M.; Nagashima, K.; Yoshida, H.; Kanai, M.; Gang, M.; Anzai, H.; Zhuge, F.; Yong, H.; Boudot, M. et al. Rational concept for reducing growth temperature in vapor-liquid-solid process of metal oxide nanowires. *Nano Lett.* **2016**, *16*, 7495–7502.

[18] Zhang, H. D.; Yu, M.; Zhang, J. C.; Sheng, C. H.; Yan, X.; Han, W. P.; Liu, Y. C.; Chen, S.; Shen, G. Z.; Long, Y. Z. Fabrication and photoelectric properties of La-doped p-type ZnO nanofibers and crossed p–n homojunctions by electrospinning. *Nanoscale* **2015**, *7*, 10513–10518.

[19] Liu, S.; Liu, S. L.; Long, Y. Z.; Liu, L. Z.; Zhang, H. D.; Zhang, J. C.; Han, W. P.; Liu, Y. C. Fabrication of p-type ZnO nanofibers by electrospinning for field-effect and rectifying devices. *Appl. Phys. Lett.* **2014**, *104*, 042105.

[20] Kim, S.; Carpenter, P. D.; Jean, R. K.; Chen, H. T.; Zhou, C. W.; Ju, S.; Janes, D. B. Role of self-assembled monolayer passivation in electrical transport properties and flicker noise of nanowire transistors. *ACS Nano* **2012**, *6*, 7352–7361.

[21] Hong, W. K.; Sohn, J. I.; Hwang, D. K.; Kwon, S. S.; Jo, G.; Song, S.; Kim, S. M.; Ko, H. J.; Park, S. J.; Welland, M. E. et al. Tunable electronic transport characteristics of surface-architecture-controlled ZnO nanowire field effect transistors. *Nano Lett.* **2008**, *8*, 950–956.

[22] Zou, X. M.; Liu, X. Q.; Wang, C. L.; Jiang, Y.; Wang, Y.; Xiao, X. H.; Ho, J. C.; Li, J. C.; Jiang, C. Z.; Xiong, Q. H. et al. Controllable electrical properties of metal-doped In_2O_3 nanowires for high-performance enhancement-mode transistors. *ACS Nano* **2013**, *7*, 804–810.

[23] Wang, F. Y.; Yip, S. P.; Dong, G. F.; Xiu, F.; Song, L. F.; Yang, Z. X.; Li, D. P.; Hung, T. F.; Han, N.; Ho, J. C. Manipulating III-V nanowire transistor performance via surface decoration of metal-oxide nanoparticles. *Adv. Mater. Interface* **2017**, *4*, 1700260.

[24] Zou, X. M.; Wang, J. L.; Liu, X. Q.; Wang, C. L.; Jiang, Y.; Wang, Y.; Xiao, X. H.; Ho, J. C.; Li, J. C.; Jiang, C. Z. et al. Rational design of sub-parts per million specific gas sensors array based on metal nanoparticles decorated nanowire enhancement-mode transistors. *Nano Lett.* **2013**, *13*, 3287–3292.

[25] Zhang, X. W.; Zhang, X. J.; Wang, L.; Wu, Y. M.; Wang, Y.; Gao, P.; Han, Y. Y.; Jie, J. S. ZnSe nanowire/Si p–n heterojunctions: Device construction and optoelectronic applications. *Nanotechnology* **2013**, *24*, 395201.

[26] Long, Y. Z.; Yu, M.; Sun, B.; Gu, C. Z.; Fan, Z. Y. Recent advances in large-scale assembly of semiconducting inorganic nanowires and nanofibers for electronics, sensors and photovoltaics. *Chem. Soc. Rev.* **2012**, *41*, 4560–4580.

[27] Cao, J.; Dou, H. M.; Zhang, H.; Mei, H. X.; Liu, S.; Fei, T.; Wang, R.; Wang, L. J.; Zhang T. Controllable synthesis and HCHO-sensing properties of In_2O_3 micro/nanotubes with different diameters. *Sens. Actuators B Chem.* **2014**, *198*, 180–187.

[28] Liu, H. Q.; Reccius, C. H.; Craighead, H. G. Single electrospun regioregular poly(3-hexylthiophene) nanofiber field-effect transistor. *Appl. Phys. Lett.* **2005**, *87*, 253106.

[29] Teo, W. E.; Ramakrishna, S. A review on electrospinning design and nanofibre assemblies. *Nanotechnology* **2006**, *17*, R89-R106.

[30] Wu, H.; Lin, D. D.; Zhang, R.; Pan, W. ZnO nanofiber field-effect transistor assembled by electrospinning. *J. Am. Ceram. Soc.* **2008**, *91*, 656–659.

[31] Choi, S. H.; Jang, B. H.; Park, J. S.; Demadrille, R.; Tuller, H. L.; Kim, I. D. Low voltage operating field effect transistors with composite In_2O_3-ZnO-$ZnGa_2O_4$ nanofiber network as active channel layer. *ACS Nano* **2014**, *8*, 2318–2327.

[32] Gazquez, G. C.; Lei, S. D.; George, A.; Gullapalli, H.; Boukamp, B. A.; Ajayan, P. M.; ten Elshof, J. E. Low-cost, large-area, facile, and rapid fabrication of aligned ZnO

nanowire device arrays. *ACS Appl. Mater. Interfaces* **2016**, *8*, 13466–13471.

[33] Zhao, C. H.; Huang, B. Y.; Xie, E. Q.; Zhou, J. Y.; Zhang, Z. X. Improving gas-sensing properties of electrospun In_2O_3 nanotubes by Mg acceptor doping. *Sens. Actuators B Chem.* **2015**, *207*, 313–320.

[34] Meng, Y.; Liu, G. X.; Liu, A.; Guo, Z. D.; Sun, W. J.; Shan, F. K. Photochemical activation of electrospun In_2O_3 nanofibers for high-performance electronic devices. *ACS Appl. Mater. Interfaces* **2017**, *9*, 10805–10812.

[35] Kim, G. H.; Jeong, W. H.; Ahn, B. D.; Shin, H. S.; Kim, H. J.; Kim, H. J.; Ryu, M. K.; Park, K. B.; Seon, J. B.; Lee, S. Y. Investigation of the effects of Mg incorporation into InZnO for high-performance and high-stability solution-processed

thin film transistors. *Appl. Phys. Lett.* **2010**, *96*, 163506.

[36] Liu, G. X.; Liu, A.; Zhu, H. H.; Shin, B.; Fortunato, E.; Martins, R.; Wang, Y. Q.; Shan, F. K. Low-temperature, nontoxic water-induced metal-oxide thin films and their application in thin-film transistors. *Adv. Funct. Mater.* **2015**, *25*, 2564–2572.

[37] Zhang, F.; Liu, G. X.; Liu, A.; Shin, B.; Shan, F. K. Solution-processed hafnium oxide dielectric thin films for thin-film transistors applications. *Ceram. Int.* **2015**, *41*, 13218–13223.

[38] Ko, J.; Kim, J.; Park, S. Y.; Lee, E.; Kim, K.; Lim, K. H.; Kim, Y. S. Solution-processed amorphous hafnium-lanthanum oxide gate insulator for oxide thin-film transistors. *J. Mater. Chem. C* **2014**, *2*, 1050–1056.